General EPR pattern from molecular hydrino produced in various reactors

Wilfred R. Hagen[a,*], Randell L. Mills[b,*]

[a] Department of Biotechnology, Delft University of Technology, Delft, The Netherlands
w.r.hagen@tudelft.nl
[b] Brilliant Light Power Inc, Cranbury, NJ, USA
rmills@brilliantlightpower.com

ABSTRACT

Hydrino, H(1/p), is any small form of atomic hydrogen with state energy $E_n = -13.598/n^2$ eV, in which n = 1/p, and p is a limited integer $1 < p \leq 137$. Electron transition to a hydrino state is non-radiative and requires a quantized amount of energy, $2mE_1$ (m is integer) to be transferred to a catalyst. Furthermore, hydrino can dimerize to molecular hydrino, $H_2(1/p)$, by loss of its bond energy, e.g., to a reaction wall. In contrast to molecular hydrogen, molecular hydrino is paramagnetic with S = 1/2. We have previously reported a uniquely sharp multi-line EPR spectrum for gaseous molecular hydrino included in spheres of gallium oxide hydroxide, $H_2(1/4)$@Ga(O)OH, which was produced in a plasma discharge reactor with gallium as an electrode and nascent water as the catalyst. Contrarily, EPR spectra of a very different nature are exhibited by $H_2(1/4)$ produced in multiple reactors of different type. Broad-line powder patterns are observed extending from 0 to some 8000 Gauss in dual-mode X-band. Unusual temperature dependence include anti-Curie behaviour and a magnetic phase transition around 107 K. Frequency-dependent resonance conditions are identified in L-, S-, X-, and Q-band. The broad EPR is analyzed in terms of a temperature-dependent dimer-of-dimers to dimer equilibrium of molecular hydrino interstitially included in the microcrystals of powder hosts. The room-temperature EPR provides a simple fingerprint identification tool to monitor the production of molecular hydrino in stable catchers.

Keywords: hydrino; EPR; nascent water; phase transition; dimer of dimers; interstitial defect

Highlights:

- New ball-mill methodology for the production of molecular hydrino
- Dual-mode and multi-frequency characterization of molecular hydrino EPR
- Unprecedented temperature behaviour includes a magnetic phase transition
- Interpretation of EPR patterns in terms of dissociating dimers of molecular hydrino
- New general EPR signature for molecular hydrino

* Corresponding authors

1. Introduction

The energy levels of the hydrogen atom are quantized as a function of the positive integer principle quantum number n,

$$E = E_0/n^2 \tag{1}$$

The ground state with n = 1 has energy E_0 = -13.6 eV. Hydrogen can transform from any state n_1 into any state n_2 by absorption ($n_1 < n_2$) or emission ($n_1 > n_2$) of light with frequency ν according to

$$h\nu = \Delta E = E_0\left[\left(\frac{1}{n_2}\right)^2 - \left(\frac{1}{n_1}\right)^2\right] \tag{2}$$

It has been hypothesized in the Grand Unified Theory of Classical Physics (GUTCP) [1] (see also refs 1-11 in [2]), and extensively experimentally corroborated ([2] and refs 13-70 therein), that the n = 1 state is in fact metastable, and that, in an action in which light is not involved, hydrogen can reach lower energy states characterized by a fractional quantum number n, which is a function of a positive integer p as

$$n = 1/p \text{ , with } 2 \le p \le 137 \tag{3}$$

An atom in any of these reduced-energy states is a 'small' hydrogen, called a *hydrino*, for which the Bohr radius a_H = 52.9 pm is reduced to a_H/p. It can be produced in a non-radiative process that proceeds according to the reaction

$$m \times 27.2 \text{ eV} + \text{H}(1) + \text{Cat} \rightarrow \text{H}^*[1/(1+m)] + \text{Cat}^* + m \times 27.2 \text{ eV} \tag{4}$$

in which m = p – 1, Cat is a catalyst that becomes excited, by resonant ionization, to Cat* by absorption of the energy on the left, m × 27.2 eV, and H* is a hydrino intermediate formed from H(1) by release of the energy on the right, m × 27.2 eV. Cat* is regenerated to Cat by release of its ionization energy. H* decays to stable H(1/p) with release of energy such that the overall reaction liberates

$$\Delta E = [(m+1)^2 - 1] \times 13.6 \text{ eV} \tag{5}$$

and reaction (4) may be written as

$$\text{H}(1) \rightarrow \text{H}(1/p) + (p^2 - 1) \times 13.6 \text{ eV} \tag{6}$$

Atomic hydrino H(1/p) may dimerize into molecular hydrino H_2(1/p) by collision with a third body, such as a reactor wall, to remove the bond energy.

We have recently studied molecular hydrino with EPR spectroscopy [2] because it was hypothesized in the GUTCP (ch 16.7 of [1]) to be paramagnetic. Specifically, on the basis of the GUTCP model for the electron, the molecule H_2(1/4) was predicted to carry a diamagnetic and a paramagnetic electron in mutual spin-orbit interaction, resulting in an EPR peak with g = 2.00464, which was furthermore predicted to be split into a unique and detailed fine structure. In particular, the line should be split by spin-orbit interaction into two lines separated by 3.99 Gauss. In turn each of these lines should exhibit a sub-line pattern with a separation of 0.311 Gauss as a consequence of linkage of magnetic flux by the paramagnetic electron in units of the magnetic flux quantum ϕ_0 = h/2e. Additionally, relative rotation of the two electrons quantized in terms of m integer units of ħ afforded extra pairs of lines around g = 2.00464 with splitting ±m × 2 × 3.99 Gauss, where,

furthermore, each of the satellites would be split through the linkage of magnetic flux during a spin transition [2]. This very detailed pattern was virtually quantitatively reproduced in experimental X-band EPR spectra, with very narrow Gaussian line width of 0.17 Gauss [2]. The $H_2(1/4)$ samples used in this study were prepared according to a specific variant of Equation (4) in a SunCell^R plasma reactor with molten gallium as one of the electrodes, as outlined in Figure 1.

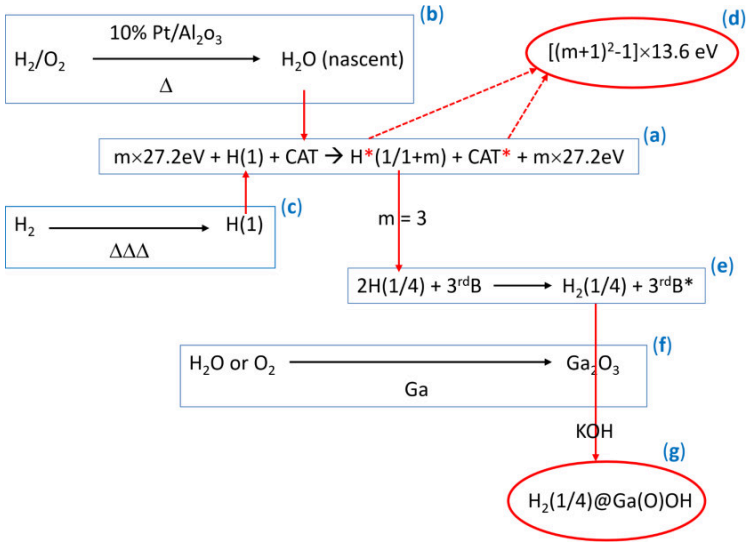

Fig. 1 – Production scheme of molecular hydrino trapped in gallium oxide hydroxide cages. (a) the catalyst for the hydrino reaction, nascent HOH, and atomic hydrogen are produced over a Pt catalyst from molecular hydrogen and oxygen gas recombination and hydrogen dissociation, respectively; (b) atomic hydrino is catalytically produced from atomic hydrogen by a nonradiative energy transfer to HOH to form an ionized catalyst state and hydrino in an energetic unstable intermediate state; (c) high energy is generated when the hydrino intermediate converts to stable hydrino, and the ionized catalyst recombines to its initial form wherein high power is released that maintains a plasma in the reaction cell chamber which increases the concentration of atomic hydrogen and catalyst to greatly increase the power and intensify the plasma; (d) two hydrino atoms combine into molecular hydrino by collision with a third body; (e) gallium oxide is formed from gallium metal in the presence of water or oxygen gas; (f) aqueous KOH treatment leads to inclusion of molecular hydrino gas in hexagonal gallium oxide hydroxide to form white fibers that float on the surface of the solution. The end product for m = 3, that is, p = 4, $H_2(1/4)$@Ga(O)OH, affords a unique S = 1/2 EPR spectrum.

The catalyst is nascent water, that is, water not hydrogen-bound to other water molecules, and the produced molecular hydrino, $H_2(1/4)$ is physiosorbed to gallium oxide, and subsequently becomes entrapped in gallium oxide hydroxide cages with conversion of the Ga_2O_3 into Ga(O)OH. TEM analysis showed the hydrino-associated gallium oxide hydroxide to differ from conventional Ga(O)OH in its crystal form (hexagonal versus orthorhombic) and its sensitivity for electron-beam disintegration (very sensitive versus insensitive). SEM analysis of the $H_2(1/4)$@Ga(O)OH showed chains of microscopic sphere-like particles of 100 nm average diameter [2]. The hydrino is hypothesized to be included in these particles as a low-pressure gas consistent with the reproducible observation of the very small EPR line width from multiple solid samples measured at ambient temperature.

In spite of the straightforward identification of $H_2(1/4)$ on the basis of the remarkable correspondence of its detailed and unique EPR spectrum with prediction from GUTCP, our follow-up studies elucidated an important discovery. Although molecular hydrino can be produced in variety of

ways, it appeared that only the procedure of Figure 1 afforded the sharp multi-line spectrum. All other methods tested did not result in an EPR signal under the measuring conditions employed for the H_2(1/4)@Ga(O)OH samples. In the present work we show that samples from other methods all give rise to mutually similar EPR properties, which, however, are completely different from the H_2(1/4)@Ga(O)OH EPR, thus attesting to the fact that the physical state of molecular hydrino in these samples is fundamentally different form the low-pressure gas state. Based on a comprehensive analysis of EPR data, below, we will make the case for paramagnetic hydrino dimer molecules that lock into non-magnetic dimers of dimers at a magnetic phase transition temperature as interstitial defects of their host materials.

2. Material and methods

2.1. Sample preparation

Generally, samples for EPR spectroscopy were produced in two different ways, 'web samples' by wire detonation to propagate a plasma explosion, and 'mill samples' by high-energy impact ball milling. In all cases nascent water was the catalyst.

Method-1 (plasma explosion): samples comprising solid web-like fibers were prepared by wire detonation of an ultrahigh purity Me wire (Me = Ti, Zn, Mo, Ag) in a rectangular cuboid Plexiglas chamber having a length of 46 cm and a width and height of 12.7 cm. Typically, a 10.2 cm long, 0.25 mm diameter metal wire was mounted between two Mo poles with Mo nuts at a distance of 9 cm from the chamber floor, a 15 kV capacitor (Westinghouse model 5PH349001AAA, 55 F) was charged to about 4.5 kV corresponding to 557 J by a 35 kV DC power supply, and a 12 V switch with a triggered spark gap switch (Information Unlimited, model-Trigatron10, 3 kJ) was used to close the circuit from the capacitor to the metal wire inside of the chamber to detonate the wire. The detonation chamber contained air comprising 20 Torr of water vapor controlled by a humidifier and a water vapor sensor. The water vapor served as a source of HOH catalyst and atomic H to form molecular hydrino. The high voltage DC power supply was turned off before closing the trigger switch. The peak voltage of about 4.5 kV was discharged as a damped harmonic oscillator over about 300 s at a peak current of 5 kA. A three-dimensional web of thin filaments or fibers formed from the atmosphere in about 3-10 minutes after the wire detonation. 'Me-web' powder samples, H2(1/4)@metaloxide, were collected from the chamber, chamber floor and chamber walls, and stored in standard EPR quartz tubes. Additionally, H2(1/4)@Ga(O)OH was prepared as base-stabilized web samples as previously described in detail [2].

Method-2 (ball milling): samples comprising mixtures of inorganic compounds of variable composition, each comprising a source of H and a source of O to form H and HOH catalyst further served as a as hydrino getter, were prepared by high-energy ball milling of each mixture. To minimize possible method-dependent introduction of artifacts, three different milling machines were employed. With a Retsch PM100 planetary ball mill intermittently reversing, 500 mL stainless steel jar, with 5 stainless steel balls (Retsch Inc, Newtown, PA) samples were typically run for 6 h at 300-400 rpm. With an Across PQ-N2 planetary ball mill, 500 mL stainless steel jar, with 5 stainless steel balls (Across International, Livingston, NJ) samples were run for 5 h at 300 rpm. And with a Nanbei NXQM-1A, 500 mL tungsten carbide jar, with 8 tungsten carbide balls (Nanbei Instruments Limited, Jinshui, Zhengzhou, PRC) samples were run for 20 h at 250 rpm.

2.2 Spectroscopy

X-band spectra were recorded at 9.4-9.9 GHz with a Bruker EMX-plus spectrometer using the high-sensitivity ER4119HS resonator. The microwave frequency was monitored with a 20 GHz Hewlett Packard 5350B frequency counter. The modulation frequency was always 100 kHz, and the

temperature was ambient (20 ^{0}C) unless indicated otherwise. Temperature-dependent studies were done using the standard ER4102ST resonator and a home-built helium flow system [3]. Background signal free quartz for sample tubes and for the flow dewar were obtained from QSIL GmbH Quarzschmelze Ilmenau, Germany. Sample temperature was measured with a carbon-composition thermometer [4] placed inside the sample just above the cavity measuring area. Q-band data were taken at ca 35 GHz with a Varian E-line spectrometer with the recorder y-axis amplitude and the x-axis micro switches connected to a NI 6001 data acquisition interface (National Instruments) for 20 kS/s digital storage using a LabVIEW program. A WR-28 waveguide 566-series cross guide directional coupler combined with a 410-series waveguide to coax transition (Millimeter Wave Products) were built into the main microwave path of the Q-band bridge to monitor the frequency with a 46 GHz Hewlett Packard 5352B frequency counter. L- and S-band spectra at ca 1.4 and 4.1 GHz were collected with the home-built broadband extension to the Bruker EMX-plus spectrometer, as described in detail in [5,6].

3. Results and discussion

3.1 General EPR pattern

The employed methods for the production of molecular hydrino give rise to two types of samples with mutually very different EPR signals. The method used in our previous study [2] generates samples with an extremely well resolved, highly reproducible, gas-phase EPR signal consisting of many lines. The signal is reproduced from [2] as the red trace, and red inset trace, in Fig 2.

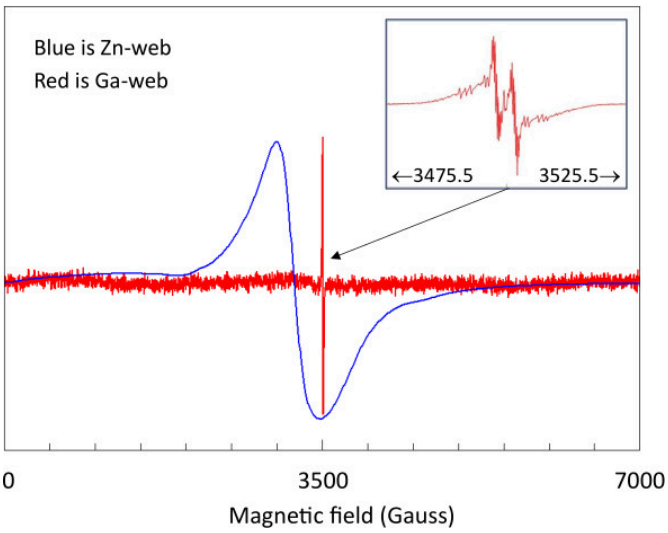

Fig. 2 – Two very different types of EPR spectra from molecular hydrino samples. The blue signal is $H_2(1/4)@Zn(OH)_2$ prepared by plasma explosion as described in Section 2.1 Sample preparation. The spectrum is exemplary for many different samples studied in this paper. It consists of a broad, asymmetric feature centered around g >2, with shouldering features, and with extra feature(s) extending into zero field. The signal is assigned (see below) to a dimer of $H_2(1/4)$. The red signal is from $H_2(1/4)@Ga(O)OH$ prepared by plasma reaction in a SunCell [7] with molten gallium as one of the electrodes, followed by workup in concentrated KOH as described in [2]. The spectrum is unique for samples prepared according to this method. The signal is assigned to included low-pressure gas of $H_2(1/4)$.

In the present work we comprehensively (re-)studied all our samples produced for hydrino EPR spectroscopy between mid-2019 and mid-2024, with the overall result of only two possible outcomes. The majority of samples, made with a variety of methods and chemicals, exclusively gave a very broad signal exemplified by the blue trace in Fig. 1, with no trace of the very sharp signal, given by the red trace in Fig. 1. A smaller set of samples, namely those whose production mandatorily involved the procedure of [2] with molten gallium as electrode, exclusively gave the very sharp signal in red in Fig. 1, with no trace of a broad blue-trace signal. Clearly, the sharp signal is only obtained with a very specific preparation procedure, and this is consistent with our previous analysis that these $H_2(1/4)$@Ga(O)OH samples have a unique structure of hexagonal Ga(O)OH crystal symmetry with chains of ca 100 nm spheres enclosing low-pressure molecular hydrino gas [2].

Initial detections of the broad signals were provisionally interpreted as arising from contaminants, and after the first observations were made of the sharp signal, early 2020, subsequent Covid-19 lockdown not only led to a standstill of new sample production, but serendipitously also created optimal conditions for in-dept study of the sharp-signal samples: the laboratory in Delft closed for all but a few experienced senior researchers, providing them essentially unlimited spectrometer access, although only no-risk experiments were permitted, which implied exclusion of cryogenics. Collection of the intrinsically weak sharp signals required unusually long data averaging times at ambient temperature. This historical context caused a delay of several years in the re-evaluation of the significance of broad signals. It has indeed only recently become apparent to us that virtually all other samples exhibit broad signal type spectra.

An orientational overview of EPR spectral patterns from different samples is presented in the next two figures. Fig. 3 shows results from plasma explosions using different metals converted into their oxides in the form of powders containing molecular hydrino.

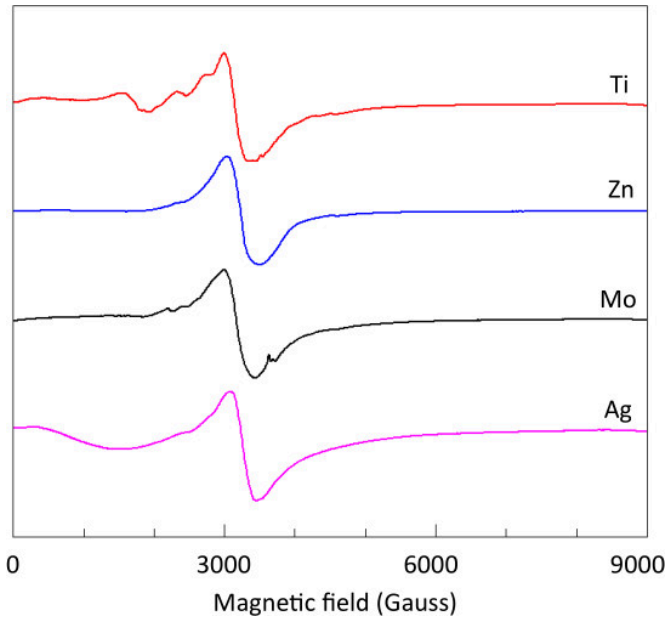

Fig.3 – Similarities in EPR spectra from filamentous web samples produced in plasma explosions with different metals as detonation wires. The overall pattern is that of a broad derivative feature around g ≈ 2.2 with shoulders on both sides and with additional features at lower fields extending into zero field. EPR conditions: microwave frequency, 9.86 GHz; modulation amplitude, 10 Gauss; temperature, 293 K.

Common denominator is a broad, asymmetric derivative-shaped feature with zero crossing at g ≈ 2.2, flanked on both sides by shoulders, and with feature(s) extending into zero field. This broad signal is reminiscent of a type of spectrum that has been frequently observed with superparamagnetic nanoparticles of iron oxides from synthetic [8], environmental [9], or biochemical [10] origin. Therefore, control experiments to exclude these sources in the present experiments are of the essence (see below).

Apparent variability of 'the' broad signal is illustrated in Fig. 4 on multiple experiments with zinc hydroxide as the carrier of molecular hydrino.

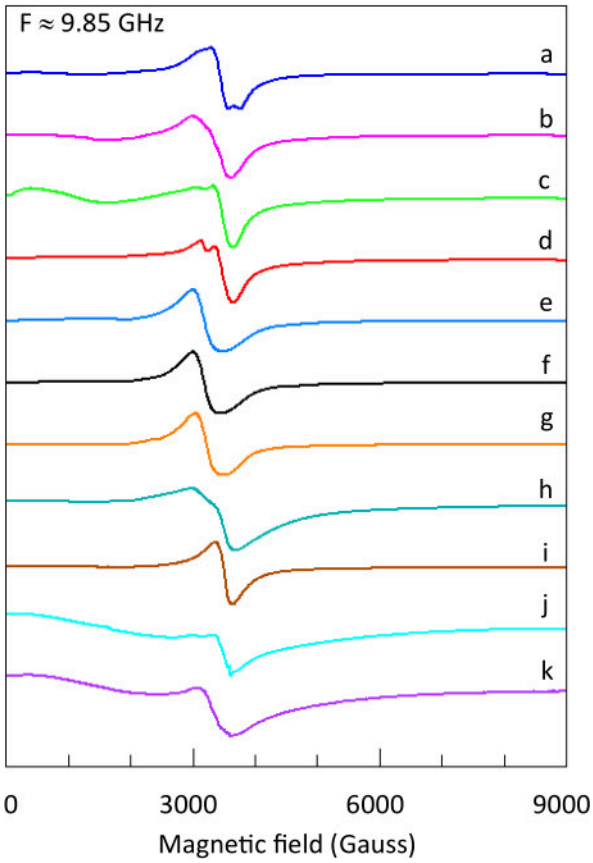

Fig.4 – Variations in the broad X-band EPR spectra from different samples of H_2(1/4) associated with ZnO or $Zn(OH)_2$. Zn-web samples a-g were produced over a 17 months period in different plasma runs. Samples h-k were produced in a Retsch stainless steel planetary ball mill. Their starting composition (weight %) was, respectively, $Zn(OH)_2$/KCl (50/50); ZnO/NaCl/$NaHCO_3$ (33/33/33); $Zn(OH)_2$/KCl/Ga (47.5/47.5/5); and ZnO/NaCl/$NaHCO_3$/Ga (31.6/31.6/31.6/5). EPR conditions: microwave frequency, 9.84-9.86 GHz; modulation amplitude, 10 Gauss; temperature, 295 K.

The subtle, and not so subtle, variations in Fig. 4 point towards the necessity to develop a theoretical explanation of diversity in the broad signal's spectral details. Note that all chemicals used in these hydrino generating reactions are diamagnetic, and that multiple reports on EPR of ZnO nanoparticles (for example, [11-14]) refer to defects that typically generate spectra very different from the ones in Fig. 4. ZnO nanoparticles can produce broad EPR spectra somewhat similar to those in Fig. 4, but only when doped with $\gtrsim$ 2.5% (with respect to Zn) paramagnetic metal ions that afford ferromagnetic/superparamagnetic resonance, e.g., Mn(II) [15], Fe(III) [16], Co(II) [17].

3.2 Control experiments

The variations of the broad signal, as exemplified in Fig. 4 and 5, are similar to X-band EPR spectra published for $Fe_2O_3 \cdot H_2O$ nanoparticles of environmental, synthetic, or biological origin [8-10]. In those systems the origin of the signal is ascribed to arrays of high-spin Fe^{3+}, S = 5/2, ions that align in the superparamagnetic phase of (anti)ferromagnetic (poly)crystals with mutual exchange interaction between the iron ions. Such systems can be described with classical-physics concepts, e.g., in terms of a bulk anisotropic magnetic susceptibility (e.g., [8,18-20]), and alternatively in quantum physics, in terms of a spin Hamiltonian, whereby the spin of the system is a resultant of all individual ion spins and their exchange interactions [21-26]. The value of this system spin is typically much higher than individual-ion spins, and is denoted by big spin or giant spin. Typical temperature dependence of the EPR intensity (or the magnetic susceptibility) is a sharp increase with increasing T, levelling off at intermediate T, and then a more shallow decrease towards room temperature for nanoparticles [8,9], molecular magnets [27,28], or ferritin protein [18,25].

By inference one could hypothesize that the EPR spectra reported here, reflect some form of agglomeration of a large number of S = 1/2 spins from individual hydrino, $H_2(1/4)$, molecules enclosed in a polycrystalline carrier of metal (hydr)oxide and/or salt. This hypothesis by analogy immediately suggests a number of follow-up experiments. Characteristic temperature-dependence should be observable with an intensity maximum at intermediate T. Furthermore, characteristic multi-frequency EPR should be observable, possibly reflecting details of the zero-field interaction. Finally, control experiments are called for to exclude that the here observed signals are due to contaminations by conventional superparamagnets for example due to iron resulting from damaged stainless steel ball mills or from impure hydrino getter or matrix chemicals. We start with the latter (Fig. 5).

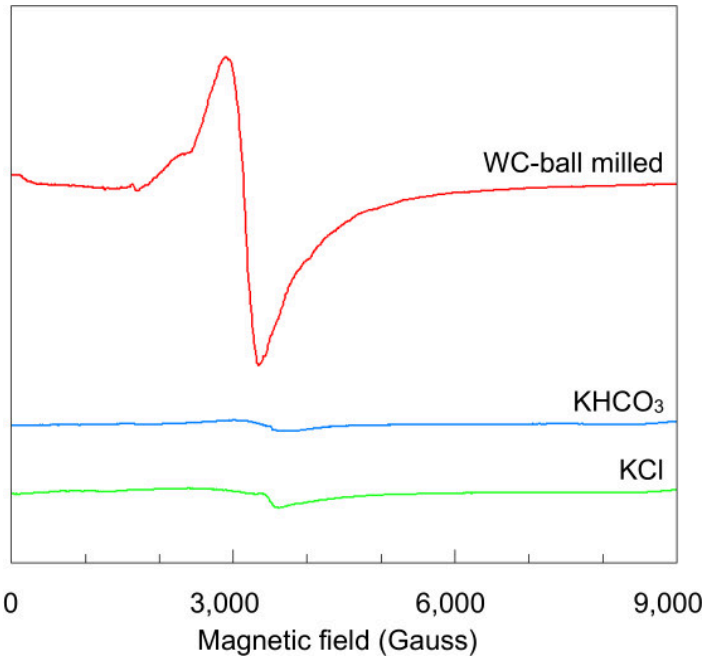

Fig. 5 – Control experiment showing the generation of the broad EPR signal of H_2(1/4) in a sample produced in a tungsten carbide ball mill. The test shows that the signal is not associated with iron contamination from the mill, nor from contaminants in the original chemicals. EPR conditions: microwave frequency, 9.84 GHz; modulation amplitude, 10 Gauss; temperature, 293 K.

Figure 5 shows an ambient temperature spectrum from a sample of $KHCO_3$/KCl (50/50% in weight) ball-milled in a container made of tungsten carbide, WC, with balls also made of tungsten carbide. The figure also features baseline spectra from the original ingredients, $KHCO_3$ and KCl before milling. Generation of a broad signal is qualitatively independent of the type of ball-milling machine (cf. the results of ball-milling with stainless-steel equipment used for traces h-k in Figure 4). The original chemicals in pure form exhibit only weak background signals. By and large, we conclude that broad signals assignable to molecular H_2(1/4) aggregates can be generated by multiple variants of two very different methods of plasma ignition versus ball-milling, and that the EPR measurements are essentially not due to background signals in the starting materials. We can now check for other predicted EPR properties of giant-spin systems.

3.3 Dual-mode EPR

At sufficiently low magnetic field B_0 the high-field selection rule $|\Delta m_S| = 1$ for allowed EPR transitions will no longer be strictly valid due to level mixing by the zero-field interaction. In high-field notation the selection rule softens to $|\Delta m_S| = 1, 2$, etc., and EPR intensity may now also be detected in parallel mode, that is, for the magnetic component of the microwave $B_1 \parallel B_0$ [29,30]. In the present work we took two samples from the two different methods (plasma explosion versus ball milling) with relatively strong regular-mode ($B_1 \perp B_0$) EPR amplitude to check for intensity in parallel mode (Figure 6).

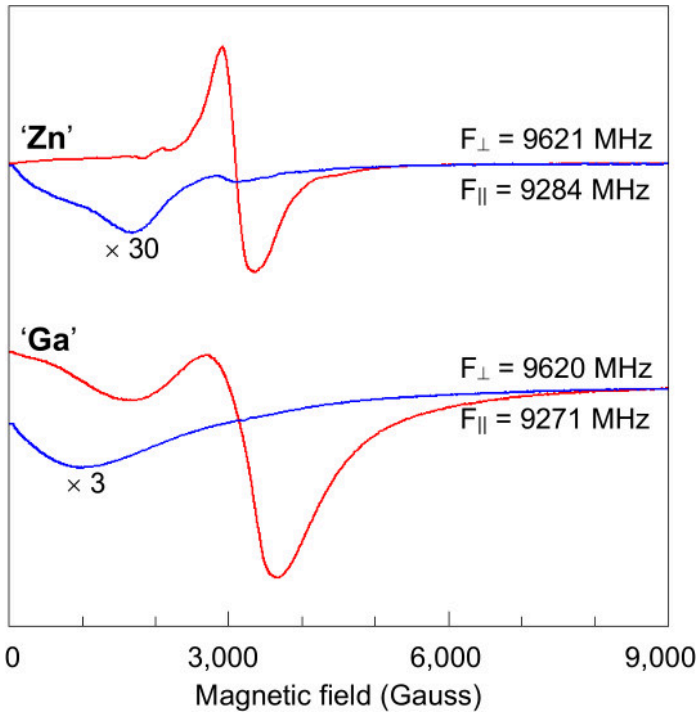

Fig. 6 – Perpendicular-mode (red traces) and parallel-mode EPR of molecular hydrino in two different samples. 'Zn' is $H_2(1/4)@Zn(OH)_2$ or molecular hydrino produced in a Zn plasma explosion. 'Ga' is molecular hydrino produced in a ball-mill experiment in which the starting material was $NaHCO_3$/NaCl/Ga as 47.5/47.5/5 wt%, which was treated in a Retsch stainless steel mill for 6 hours at 300 rpm. Experimental EPR conditions: perpendicular- and parallel-mode frequencies as indicated; modulation amplitude, 10 Gauss; microwave power, 32 mW; temperature, 293 K. The amplitude of the parallel-mode spectrum has been multiplied by a factor 30 ('Zn') or 3 ('Ga') compared to the perpendicular-mode spectrum.

As in all previous spectra (Figs 1- 5) both samples have perpendicular-mode spectral features at low field extending into zero field. In parallel mode the central $|\Delta m| = 1$ line around $g \approx 2.1–2.2$ is strongly suppressed, making the low-field features stand out and suggesting them to stem from $|\Delta m| \neq 1$ transitions. The shapes are different from their equivalents in perpendicular mode. Also, they start off from zero field at or below the baseline and with a negative slope, suggesting that (more than) half of these features has disappeared into zero field.

3.4 Multi-frequency EPR

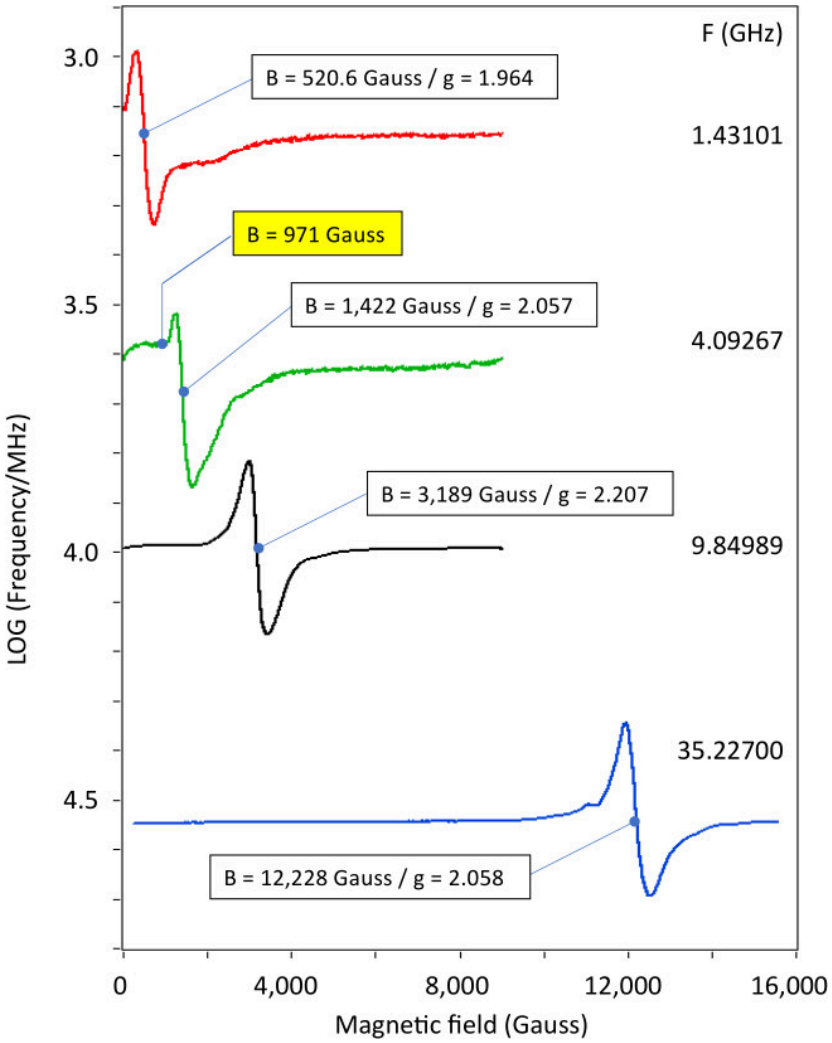

Fig. 7 – Multi-frequency spectra of the H_2(1/4)@Zn(OH)$_2$ compound of Fig. 6. EPR conditions: the L-(1.43101 GHz) and S-band (4.09267 GHz) spectra were taken with a modulation amplitude of 25 Gauss and were 9 times averaged; X-band EPR (9.62135 GHz) was as in Fig. 6; for Q-band (35.22700 GHz) the modulation amplitude was 10 Gauss and the microwave power was 12.6 mW. All spectra were taken at a temperature of 293 K. Positions of the zero crossing of the main line and of a special inflection point (S-band: in yellow, see section 3.6) are indicated.

The two samples of Figure 6 were studied in regular-mode multi-frequency EPR. Data for the 'Zn' sample are in Figure 7. Increasing the frequency makes the Zeeman interaction more dominant over zero-field interaction, if present. Consequently, data at higher frequencies may afford more accurate determination of g values. Contrarily, decreasing the frequency makes possible zero-field interaction stand out with respect to the Zeeman interaction.

Remarkably, the apparent g value, that is, the zero crossing of the main line around $g \approx 2$ is not a constant. Another interesting observation is that the line width of the main line only slightly decreases with decreasing frequency. These combined facts should be key factors in any interpretation of the EPR as they do not appear to be easily compatible with conventional low-spin, high-spin, or giant-spin models. A frequency-dependent g shift could originate in higher-order terms

in the magnetic field, e.g., of the form SB^3 [31], and many of these terms would be theoretically allowed for a giant spin of low symmetry [32], however, limited experimental results indicate that very high fields are required for measurable effects at least in single-ion systems [33]. A constant line width implies that the broadening is either caused by a field independent interaction such as a random distribution in zero-field parameters, or/and it reflects an essentially frequency-independent relaxation.

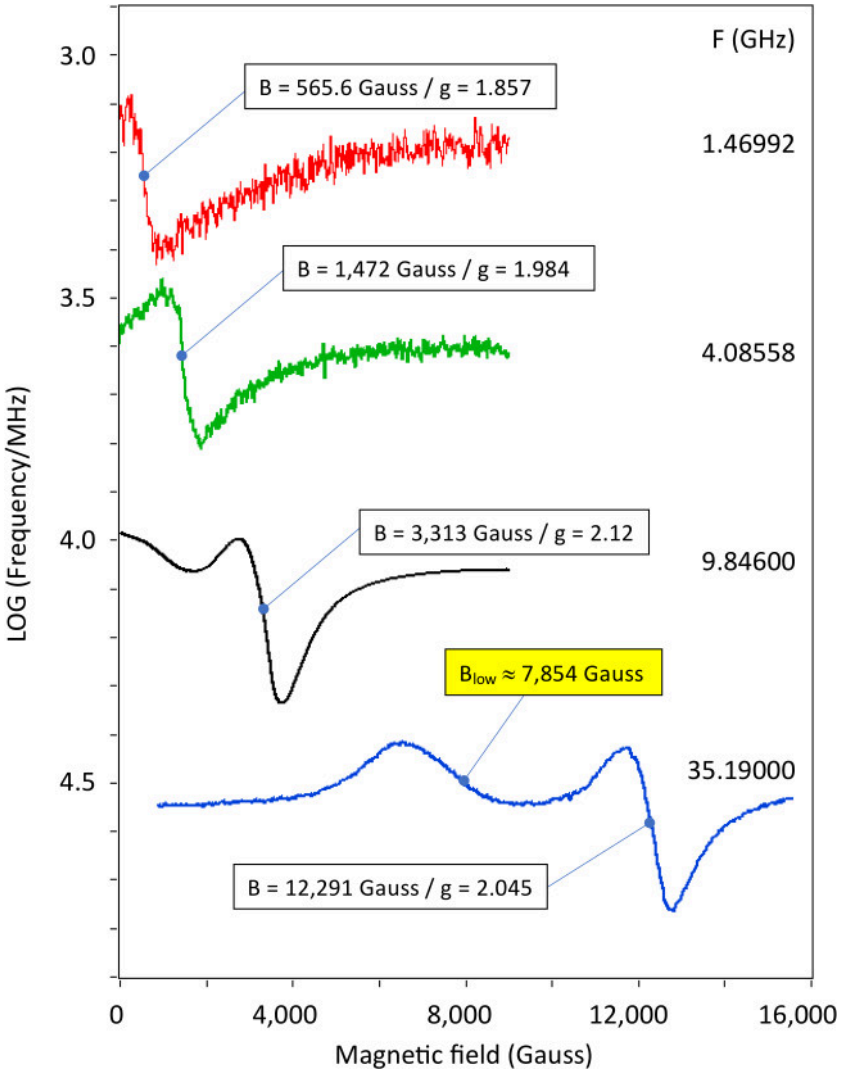

Fig. 8 – Multi-frequency spectra of the compound $NaHCO_3$/NaCl/Ga 47.5/47.5/5 wt% of Fig. 6. EPR conditions were as in Fig. 7; frequencies are given in the figure. Positions of the zero crossing of the main line and of an extra line (in yellow, see section 3.6) in Q-band are indicated.

Figure 8 gives the equivalent multi-frequency spectra for the compound $NaHCO_3$/NaCl/Ga 47.5/47.5/5 wt%. The spectral features are broader than in Fig. 7, but the overall pattern is the same: The zero crossing of the main line is not a constant, and the line width of the main line is essentially independent of the frequency. Besides, a strong zero-field feature in X-band moves to high field in Q-band while retaining its high intensity. This is another feature that is not readily compatible with simple spin models.

3.5 Temperature dependence

The H_2(1/4)@$Zn(OH)_2$ sample of Figs 6 and 7 was studied in regular X-band as a function of sample temperature from 292 K down to 8 K. Fig. 9, panel A, shows selected spectra for 'high' temperatures down to 116 K. Remarkably, the signal is not constant in shape: significant variations occur in the shoulders of the main peak and also in the low-field region of $|\Delta m_S| > 1$ transitions. Even the main peak itself exhibits changes in position, or apparent g value, and in width. These variations are not related to saturation; the signals do not show any saturation at all up to maximal incident power of 0 dB = 200 mW. Perhaps even more notable is the unusual relation between intensity and temperature. The signal slightly decreases with decreasing temperature over this region, where a paramagnet in an isolated ground state would rather increase according to Curie's law by a factor of 292/116. Overall, the powder pattern is qualitatively invariant until we reach a small temperature range of some 10 K around the value of $T \approx 107$ K, for which selected spectra are presented in panel B of Fig. 9. In this narrow slot drastic changes occur eventually resulting in an order-of-magnitude change in the main-peak amplitude and in a powder pattern that is essentially completely below the zero baseline, indicating that a large part of the EPR absorption spectrum has moved into zero field. From this temperature window downwards, the new overall signal is again qualitatively invariant in shape as well as in intensity, as shown in panel C of Fig. 9. The black trace in panel C (T = 97.5) is identical to the red trace in panel B. It still shows some effects of the drastic changes that took place over the ca 10 K slot around $T \approx 107$ K. At lower temperatures, however, the amplitude becomes virtually independent of the temperature. Minor changes in the shoulders of the main peak and in the low-field range are also observed here. Down to 11 K no saturation whatsoever is observed for a power range of -40 to 0 dB. Repeated cycling from room temperature down to 8 K results in fully reproducible spectra.

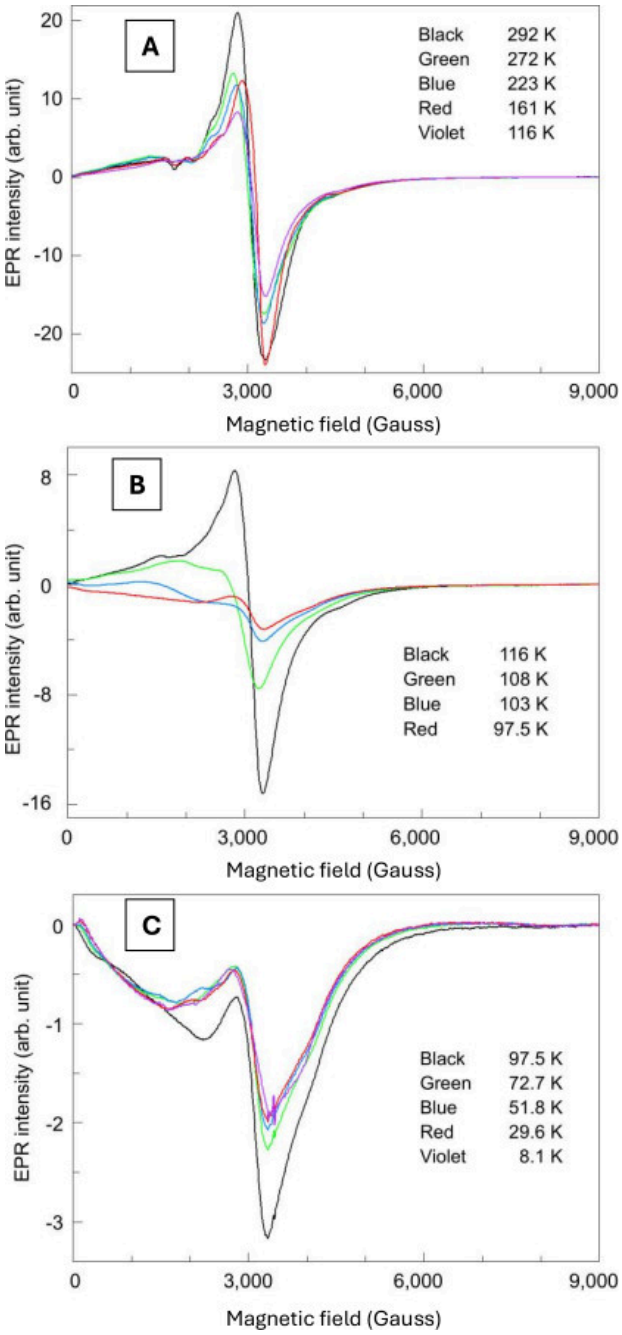

Fig. 9 – Temperature dependence of the broad X-band EPR signal form $H(1/4)_2Zn(OH)_2$ shows three different phases. Panel A, high-temperature phase in which the intensity of a relatively sharp central line only minorly decreases with decreasing temperature, accompanied by small changes in the width and position (effective g value) of the central peak, in shoulders, and in low-field features. Panel B, transition temperature range in which the spectral pattern drastically changes over a small temperature slot of ca 10 K around ca 107 K to eventually turn into the 'low-temperature' spectrum with an order-of-magnitude decrease in amplitude associated with a transfer of large part of the EPR into zero field. Panel C, low-temperature phase in which the spectral intensity is essentially invariant with the temperature, however, again with a range of small changes in shoulders and low-field features. EPR conditions: microwave frequency 9405-9406 MHz; modulation amplitude, 10 Gauss; microwave power, -4 dB, that is 80 mW (non-saturating).

A convenient way to visualize temperature dependence of EPR intensity is to plot the intensity of a signal multiplied by the temperature as a function of that temperature. For an S = 1/2 system this affords a straight horizontal line. For a low-lying excited state, e.g., an intermediate level pair in an S = n/2 system, the plot would give an S-shaped pattern reflecting population with increasing temperature at the expense of the ground state. When the spectrum changes shape as function of temperature, then the second integral of the complete spectrum can be taken as EPR amplitude. Such an approach would be problematic in the present case due to: (1) the many small variations observed; (2) the drastic change in overall spectrum associated with the T ≈ 107 K transition; and (3) the fact that all spectra show a finite absorption into zero field. We have therefore taken the following approach: The EPR intensity in the range 292-8 K is estimated from the main peak's amplitude (peak-to-trough) multiplied by the field range of these peak positions as a measure of line width. The intermediate narrow range around T ≈ 107 K is ignored as a blind spot. The result of this procedure is presented in Fig. 10.

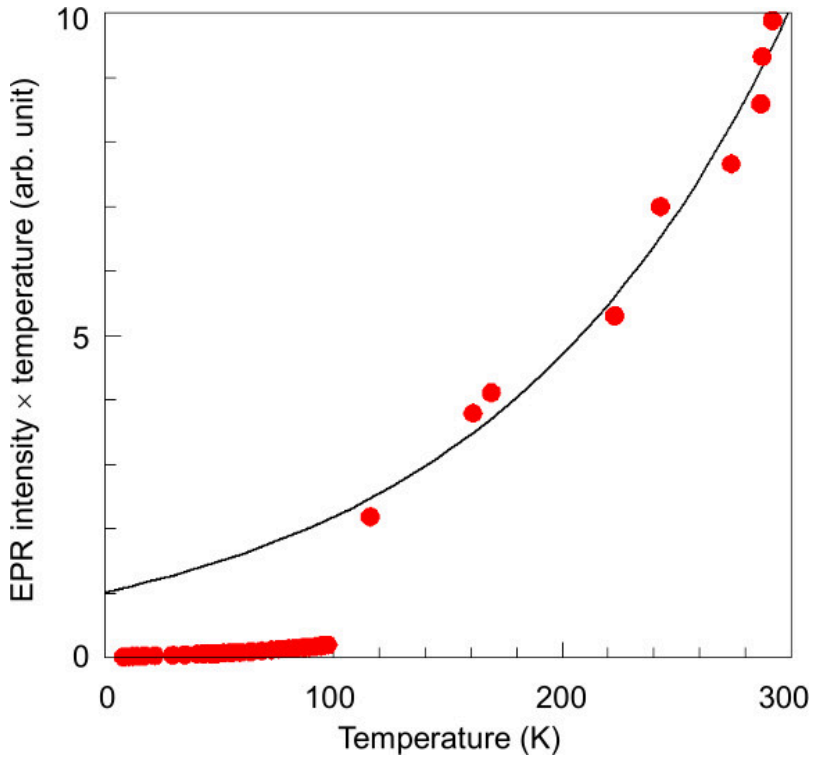

Fig. 10 – Relative population of the $H(1/4)_2@Zn(OH)_2$ paramagnet measured as EPR intensity times temperature versus temperature. For an S = 1/2 system or an isolated ground state this graph should be a straight horizontal line. EPR intensity was measured as height times width of the central line. A small transition range around 107 K is ignored. The black line is a single-exponential fit to the T ≥ 116 K data. The figure indicates that even at room temperature the spin system has not reached its maximal population by far.

Taken together, the overall temperature-corrected EPR intensity of $H_2(1/4)@Zn(OH)_2$ increases exponentially with temperature without showing any tendency to level off up to ambient temperature. There is a magnetic phase transition around T ≈ 107 K, below which the EPR intensity

collapses to a low residual level. Once more, also these observations are not readily compatible with simple spin models.

3.6 Interpretation of the combined EPR data: $\{[H_2(1/4)]_2\}_2$ dimers of dimers

It is well known that H_2 forms a linear molecular dimer at cryogenic temperatures through van der Waals bonding (chapter 16 in [1]). $H_2(1/4)$ forms a dimer as well, but due to the 4-squared higher bonding energy, the $H_2(1/4)$ dimer is stable to a much higher temperature. The molecular orbital (MO) of $H_2(1/4)$ comprises a two-dimensional prolate spheroidal equal potential, equal energy surface. The charge density of this 2-D membrane is in proportion to the distance on the membrane from the origin. Thus, the charge density is greatest at the linear poles of the molecule where the negative MO charge density is closest to the binding nuclei. Due to the axial charge distribution and its corresponding polarizability to form van der Waals binding, two $H_2(1/4)$ molecules undergo van der Waals binding to form an end-to end-linear dimer. The MO further comprises a paired and an unpaired electron, and the corresponding magnetic dipoles of the $H_2(1/4)$ dimer must have a parallel alignment coincident with the parallel van der Waals electric dipoles that bond the molecules in the linear dipole. Thus, the dimer designated $[H_2(1/4)]_2$ behaves as a spin 1/2 dipole that can only transition parallel or antiparallel to an applied magnetic field during EPR spectroscopy resulting in a single line with a Lorentzian profile. The bond energy and bond length 2c' of the dimer designated $[H_2(1/4)]_2$ given by Eqs. (16.202) and (16.205) in [1], are 0.04412 eV and $1.90575a_0$, respectively. Using the solved dimensions of $[H_2(1/4)]_2$, the energy contribution due to the aligned magnetic dipoles of $[H_2(1/4)]_2$ to the EPR spin flip transition given by Eqs. (16.252) and (16.253) in [1] is 502 Gauss downfield.

Consider the dimer that H_2 forms with $H_2(1/4)$ due to van der Waals forces. Using Eqs. (16.206) and (16.207) [1] with a normalized linear combination of the H_2 and $H_2(1/4)$ central fields and the dipole moments of (4+1)e/2 = 2.5e and 0.1334 D, the calculated $[H_2\text{-}H_2(1/4)]$ dimer bond length 2c' and bond energy given by Eqs. (16.210) and (16.213) are $3.04707a_0$ and 0.03309 eV (384 K). $H_2(1/4)\text{-}H_2$ gas as well as very large quantities of hydrogen gas are observed by gas chromatography of gas released from sources and samples of $H_2(1/4)$ wherein a mixture of H_2, $H_2(1/4)$, $H_2\text{-}H_2(1/4)$ and low amounts of $[H_2(1/4)]_2$ are present [7]. This is consistent with the high bond dissociation temperature. Sources of H_2 are from decomposition of $H_2\text{-}H_2(1/4)$ and condensation of H_2 in violation of the Clausius Clapeyron equation due to the raising of the H_2 liquefaction temperature by co-condensation with $H_2(1/4)$ [7]. Remarkably, compounds such as ZnO and Ga_2O_3 that do not ordinarily store hydrogen gas do in the presence of $H_2(1/4)$ [7].

Eq. (16.254) of [1] predicts that magnetically paired $[H_2(1/4)]_2$ dimers bond along the semiminor axis (side-to-side) by magnetic dipole bonding versus bonding along the semimajor axis (end-to-end) by van der Waals induced electric dipole bonding. At 95 K, the bond energy of 8.197×10^{-3} eV far exceeds the EPR transition energy of about 4.05×10^{-5} eV at 9.8 GHz excitation such that the dipole paired dimer has no EPR signal. The 95K transition for EPR active to inactive may be broaden to higher temperature by the confinement and effective pressure caused by the state of $[H_2(1/4)]_2$ being entrapped as inclusions in the host crystalline lattice. A dramatic decrease in the EPR signal intensity is observed (Fig. 10) at about this temperature which deceases to about 1/7.5 the intensity observed above this temperature, with a further continuous decrease to a measured temperature of 8K. This intensity-temperature relationship is anticipated considering the statistical thermodynamics of a mixture of monomer, dimer, side-to-side paired multimers and other species that increase the entropy of the system (i.e., absence of signal would require perfect side-to-side pairing of all $H_2(1/4)$ which is a very unfavorable and improbable state for an entrapped inhomogeneous mixture.). Conversely an exponentially increasing population of free $[H_2(1/4)]$ species is anticipated as function of temperature according to Maxwell–Boltzmann statistics (chapter 24 in [1]) which applies to a free gas-like state obtained at higher temperatures.

The magnetic moment of an unpaired electron is a Bohr magneton. The magnetization is the unpaired electron density times the unpaired electron magnetic moment, a Bohr magneton. Assume that each dimer occupies a cavity comprising an interstitial inclusion in a hexagonal Wurtzite ZnO lattice having aa unit-cell volume of 47.40 Å^3. To determine the unpaired electron density, consider a cylindrical volume of the radius of $H_2(1/4)$ and the length of $[H_2(1/4)]_2$ given by the sum of the internuclear distance of $[H_2(1/4)]_2$ plus the semimajor axis and internuclear distances of two $H_2(1/4)$. The volume of $[H_2(1/4)]_2$ given by Eq. (16.256) of [1] is then 0.212×10^{-31} m^3. The packing efficiency of the ZnO lattice is 74% with 26% void volume with the volume of $[H_2(1/4)]_2$ being 0.00045 times smaller. Consider the case of one $[H_2(1/4)]_2$ per hexagonal unit cell with two unpaired electrons. The unpaired electron density is then 4.2×10^{28}/m^3 . For a diamagnetic matrix, the internal magnetic field is about the magnetization times the permeability of free space. The corresponding internal magnetic field is 4917 Gauss (Eq. (16.258) of [1]). This internal magnetic field is sufficient to cause absorption of the 9.8 GHz EPR power with zero applied field (i.e. RF absorption will occur for a frequency v if the flux is greater than or equal to hv/gβ, wherein h is Planck's constant, g is the g factor, and β is the Bohr magneton).

Since the tested samples were all powders rather than magnetically aligned perfect crystals, the zero-field signal has intensity in parallel-mode (B_1 || B_0) EPR as shown in Figure 6 due to random orientations of magnetic domains that result in resonant absorption of the applied RF power for domains with a projection of the intrinsic magnetized flux vector **B** that is perpendicular to the applied RF field and satisfies the energy condition B = hv/gβ wherein the unpaired electrons respond to the internal magnetization that substitutes for the external magnetic flux. Consider an exemplary case with the applied the RF field along the z-axis. A component of magnetization along the x-axis would cause the S = 1/2 transition to be allowed. Due to variation in molecular hydrino species composition and concentration as well as magnetic domain alignment and spatial orientation relative to the applied EPR RF and B fields, a wide variation of RF absorption at zero and low field is anticipated over a range of applied RF frequencies. Zero field EPR (ZF-EPR) studies of magnetically aligned and oriented crystals is a method to determine the molecular hydrino concentration of the crystal wherein the ZF-EPR resonant frequency gives the internal field, and therefrom the density of unpaired electrons corresponding to the concentration of molecular hydrino can be determined.

The Lorentzian line width of the single EPR transition of $[H_2(1/4)]_2$ is anticipated to be much greater than that of $H_2(1/4)$ due to the requirement of the excitation field acting over the dimensions of the dimer electron current. Rather than based on Larmor precession dynamics, the line width is given by the relationship between rise time and bandwidth of electromagnetic transitions given by Eqs. (2.81-2.110) of [1]. Using Eq. (2.110)

$$\tau = 6\alpha^{-5} \cdot \frac{\hbar}{m_e c^2} \cdot \left(n_f n_i\right)^2 = 3.734826 \times 10^{-10} s \cdot \left(n_f n_i\right)^2$$

wherein n_i and n_f are the internuclear distances for $H_2(1/4)$ and $[H_2(1/4)]_2$ in units of a_0 (n_i = 0.35355 and n_f = 1.90575) corresponding to the equivalent dimensions of the wavelength of the coupled magnetic and binding van der Waals electric dipoles, the lifetime of the $[H_2(1/4)]_2$ EPR transition is 1.70 X 10^{-10} s, the corresponding frequency is 5.90×10^9 s^{-1}, and the energy width given by Planck's constant bar times the frequency is 6.22×10^{-25} J. For a g factor of 2.0046386 [2], the energy line width in Gauss is 335 Gauss which is the natural width (Eqs. (16.259-16.261) of [1]). The spin-flip energy of the EPR transition, which is typically 1000 times less than the van der Waals energy, is added to the $[H_2(1/4)]_2$ van der Waals energy to solve the semimajor axis (Eq. (16.199) in [1]) in units of a_0 which is then substituted into the transition lifetime formula (Eq. (16.259), to calculate the natural line width as a function of microwave frequency, a trivial factor effecting the natural linewidth. The natural line width is the minimum line width that may be broadened by other mechanisms such as instrument, lattice collisional, Doppler, van der Waals, Stark, resonance, inhomogeneous, and dipole broadening. Many broadening mechanisms increase with temperature.

Superposition with additional transitions such as that of $H_2(1/4)$ monomer can cause broadening and alteration of the line profile. $H_2(1/4)$ monomer may cause an upfield shoulder in the profile for example.

Multi-frequency spectra shown in Figs. 7 and 8 were recorded on the $H_2(1/4)@Zn(OH)_2$ compound and the $NaHCO_3$/NaCl/Ga compound of Fig. 6. The experimental and the theoretical EPR peak positions are given in Table 1.

Table 1. Multi-frequency results for compound 'Zn', that is $H_2(1/4)@Zn(OH)_2$ and compound 'Ga', that is $H_2(1/4)@NaHCO_3$/NaCl/Ga. Comparison of experimental and calculated peak positions.

	Frequency /GHz	Resonance field/Gauss	dipole-corrected field/Gauss	predicted peak position/Gauss	Observed peak position/Gauss
'Zn'					
	35.22700	12,573	12,071	12,071	12,288
	9.62135	3,429	2,927	2,927	3,189
	4.09267	1,458	956	956	971[a]
	1.43101	510	8	502	521[b]
'Ga'					
	35.19000	12,542	12,040		12,291
	35.19000	12,542	8,496	8,496	7,854
	9.84660	3,509	3,008		3,313
	4.08558	1,456	954		1,472
	1.46992	524	22		566

[a] EPR frequency is resonant with dipole shift within the line width; it starts with negative slope; peak position taken at zero crossing.
[b] EPR frequency is resonant with dipole shift; increased initial slope of Lorentzian line shape.

The unshifted theoretical peak positions were calculated using the formula $h\nu/g\beta$ wherein g = 2.0046386 for monomeric $H_2(1/4)$ [2]. The peak positions in all frequency bands were corrected for the predicted -502 Gauss shift due the intrinsic magnetic dipole-dipole coupling of dimeric $[H_2(1/4)]_2$. There is good agreement between the theoretical and observed positions and Lorentzian shapes of the Q-band and X-band peaks.

The 4.09267 GHz EPR frequency of the 'Zn' S-band peak is resonant with the predicted $[H_2(1/4)]_2$ magnetic dipole-dipole coupling energy of -502 Gauss within line width of ~400 Gauss consistent with the corresponding peak starting with a much lower slope than that of a Lorentzian peak. The peak position was assigned to the point at zero crossing at ca 971 Gauss. The S-band peak position and profile matches predictions. The 1.43101 GHz EPR frequency of the L-band peak is nearly exactly resonant with intrinsic magnetic dipole-dipole coupling energy of $[H_2(1/4)]_2$ corresponding to the shift of -502 Gauss. $[H_2(1/4)]_2$ dimers may undergo an external spin flip transition with a precited position of 502 Gauss while also undergoing a transition involving the intrinsic dipole-dipole coupling that is resonant with the applied frequency of 1.43101 GHz to result in an EPR peak predicted at 502 Gauss applied flux. In addition, a peak shifted by the intrinsic magnetic dipole-dipole coupling is predicted at 8 Gauss that is also resonant with the applied 1.43101 GHz. The superposition of the 8 Gauss peak and the unshifted peak is consistent with the observed peak at 521 Gauss with an increased initial slope of Lorentzian line shape due to the contribution for of the 8 Gauss transition.

Similar arguments hold for the 'Ga' compound. Furthermore, H(1/4) comprises a central field of +4e at a radius on $1/4a_0$. The field gives rise to four multipoles each of potential energy 4×27.2 eV which can resonantly accept 4×27.2 eV from another H(1/4) to form H(1/8). Two H(1/8) react to form $H_2(1/8)$, and two $H_2(1/8)$ react to form the corresponding dimer $[H_2(1/8)]_2$ (chapter 5 of [1]). The peak shifted by the predicted intrinsic magnetic dipole-dipole coupling energy of $[H_2(1/8)]_2$ was

observed in the Q band EPR of the $H_2(1/4)$@NaHCO3/NaCl/Ga sample (Fig. 8). The corresponding downfield shift of $[H_2(1/8)]_2$ is -4028 Gauss (Eqs. (16.252) and-(16.253) of [1]) that roughly matched the peak at 7,854 Gauss with the shifted peak taken at the estimated position of the zero crossing.

4. Conclusions

With the exception of the previously studied $H_2(1/4)$@Ga(O)OH, all multiple dozen samples explored in the present study afford ambient-temperature EPR spectra with a broad feature around $g \approx 2$ and extra features of lower intensity extending down to zero field. Variations occur in the intensity and the fine details of the EPR, but the overall powder pattern is similar irrespective of the hydrino getter or matrix (metal oxides or salt combinations) and the production method (plasma explosion versus ball milling). This 'broad-line' pattern' is thus a characteristic of molecular hydrino produced with nascent H_2O as the catalyst in the hydrino formation reaction. Although the pattern is somewhat reminiscent of EPR observed for different forms of ferrihydride nanoparticles (nominally $Fe_2O_3{\cdot}xH_2O$) of synthetic, environmental, or biological origin, in particular of the core of the iron storage protein ferritin, its itinerant effective g value and its specific temperature dependence are inconsistent with a giant-spin model. Furthermore, iron is absent from all samples employed in this study. Likewise, simple $S \geq 1/2$ models fail to explain the observed pattern. An $H_2(1/4)$ dimer of dimers model is proposed as follows: Two $H_2(1/4)$ form an end-to-end linear van der Waals electric dimer along the semimajor axis of the $H_2(1/4)$ MO with a spin of 1/2. Two dimers then form a side-to-side dimer-of-dimers along the semiminor axis by dipolar interaction resulting in a spin of zero at cryogenic temperatures. The dimer of dimers is an interstitial 'defect' of the host material. A magnetic phase transition sets in around a temperature of ca 107 K above which decoupling of dipolar interaction increasingly affords paramagnetic single dimers. The model semi-quantitatively explains line positions in multi-frequency EPR. In further research the present results may be combined with those of many other methodologies involving, e.g., susceptibility measurements, antiStokes and Stokes Raman spectroscopy, etc. The hydrino dimer signatures and temperature dependency are very significant. The results further indicate the production of H2(1/8) with greater release of energy than production of H2(1/4). The observation of the formation of a dimer between molecular hydrino and H2, and the temperature dependence of hydrogen release explains the massive amounts of hydrogen observed from salts containing hydrino. These salts are not known to absorb any hydrogen and indicate a new very important technology comprising the conversion of common salts to hydrogen storage materials which are potentially of great industrial value. At this time at least we have provided generally accessible routes for the production and identification of molecular hydrino.

Authors contributions

RLM developed the GUTCP theory and was responsible for the production of the samples; WRH did the EPR spectroscopy; WRH and RLM wrote the manuscript.

Declaration of competing interest

The authors declare the following financial interests/personal relationships which may be considered as potential competing interests:

Dr Mills is the founder, COE, and President of Brilliant Light Power which provided the samples. Dr Hagen has no financial or personal relationships and did not receive any financial support from Brilliant Light Power.

References

1. Mills, RL. The grand unified theory of classical physics. 2023; Vol 1, 2A, 2B, 3. www.brilliantlightpower.com/book-download-and-streaming/.
2. Hagen, WR, Mills, RL. Electron paramagnetic resonance proof for the existence of molecular hydrino. Int J Hydrogen Energy 2022; 47: 23751-23761.
3. Lundin, A, Aasa, R. A. simple device to maintain temperatures in the range 4.2-100 K for EPR measurements. J Magn Reson 1972; 8: 70-73.
4. Clement, JR, Quinnell, EH. The low temperature characteristics of carbon-composition thermometers. Rev Sci Instrum 1952; 23, 213-216.
5. Hagen, WR. Very low-frequency broadband electron paramagnetic resonance spectroscopy of metalloproteins. J Phys Chem A 2021; 125: 3208-3218.
6. Hagen, WR. Conversion of a single-frequency X-band ERP spectrometer into a broadband multi-frequency 0.1-18 GHz instrument for analysis of complex molecular spin Hamiltonians. Molecules 2023; 28: 5281.
7. Mills, RL. Hydrino states of hydrogen. https://brilliantlightpower.com/pdf/Hydrino_States_of_Hydrogen.pdf
8. Bickford, LR. Ferromagnetic resonance absorption in magnetite single crystals. Phys Rev 1950; 78: 449-457
9. Carbone, C, Di Benedetto, F, Marescotti, P, Sangregorio, C, Sorace, L, Lima, N, Romanelli, M, Lucchetti, G, Cipriani, C. Natural Fe-oxide and -oxyhydroxide nanoparticles: an EPR and SQUID investigation. Mineralogy Petrology 2005; 85: 19-32.
10. Boas, JF, Troup, GJ. Electron spin resonance and Mössbauer effect studies of ferritin. Biochim Biophys Acta 1971; 229: 68-74.
11. Orlinskii, SB, Schmidt, J, Baranov, PG, Hoffmann, DM, de Mello Donegá, C, Meijerink, A. Probing the wave function of shallow Li and Na donors in ZnO nanoparticles. Phys Rev Lett 2004; 92: 047603.
12. Zhang, Y, Xie, E. Nature of room-temperature ferromagnetism from undoped ZnO nanoparticles. Appl Phys A 2010; 99: 955-960.
13. Erdem, E. Microwave power, temperature, atmospheric and light dependence of intrinsic defects in ZnO nanoparticles: a study of electron paramagnetic resonance (EPR) spectroscopy. J Alloys Comp 2014; 605: 34-44.
14. Ghose, S, Rakshit, T, Ranganathan, R, Jana, D. Role of Zn-interstitial defect states on d^0 ferromagnetism of mechanically milled ZnO nanoparticles. RSC Adv 2015; 5: 99766.

15. Jayakumar, OD, Gopalakrishnan, IK, Kadam, RM, Vinu, A, Asthana, A, Tyagi, AK. Magnetization and structural studies of Mn doped ZnO nanoparticles: prepared by reverse micelle method. J Cryst Growth 2007; 300: 358-363.
16. Misra, SK, Andronenko, SI, Thurber, A, Punnoose, A, Nalepa, A. An X- and Q-band Fe^{3+} EPR study of nanoparticles of magnetic semiconductor $Zn_{1-x}Fe_xO$. J Magn Magn Mater 2014; 363: 82-87.
17. Hays, J, Reddy, KM, Graces, NY, Englehard, MH, Shutthanandan, V, Luo, M, Xu, C, Giles, NC, Wang, C, Thevuthasan, S, Punnoose, A. Effect of Co doping on the structural, optical and magnetic properties of ZnO nanoparticles. J Phys Condens Matter 2007; 19: 266203.
18. Wajnberg, E, El-Jaick, LJ, Linhares, MP, Esquivel, DMS. Ferromagnetic resonance of horse spleen ferritin: core blocking and surface ordering temperatures. J Magn Reson 2001; 153: 69-74.
19. Gilles, C, Bonville, P, Rakoto, H, Broto, JM, Wong, KKW, Mann, S. Magnetic hysteresis and superantiferromagnetism in ferritin nanoparticles. J Magn Magn Mater 2002; 241: 430-440.
20. Papaefthymiou, GC. The Mössbauer and magnetic properties of ferritin cores. Biochim Biophys Acta 2010; 1800: 886-897.
21. Prokof'ev, NV, Stamp, PCE. Giant spins and topological decoherence: a Hamiltonian approach. J Phys Condens Matter 1993: 5: L663-L670.
22. Fittipaldi, M, Sorace, L, Barra, A-L, Sangregorio, C Sessoli, R, Gatteschi, D. Molecular nanomagnets and magnetic nanoparticles: the EMR contribution to a common approach. Phys Chem Chem Phys 2009; 11: 6555-6568.
23. Fittipaldi, M, Innocenti, C, Ceci, P, Sangregorio, C, Castelli, L, Sorace, L, Gatteschi, D. Looking for quantum effects in magnetic nanoparticles using the molecular nanomagnet approach. Phys Rev B 2011; 83: 104409.
24. Fittipaldi, M, Mercatelli, R, Sottini, S, Ceci, P, Falvo, E, Gatteschi, D. Sensing the quantum behaviour of magnetic nanoparticles by electron magnetic resonance. Phys Chem Chem Phys 2016; 18: 3591-3597.
25. Bossoni, L, Labra-Muñoz, JA, van der Zant, HSJ, Čaluković, V, Lefering, A, Egli, R, Huber, M. In-dept magnetometry and EPR analysis of the spin structure of human-liver ferritin: from DC to 9 GHz. Phys Chem Chem Phys 2023; 25: 27694.
26. Hagen, WR. Quantum magnetism of the iron core in ferritin proteins – a re-evaluation of the giant-spin model. Molecules 2024; 29: 2254.
27. Delfs, C, Gatteschi, D, Pardi, L, Sessoli, R, Wieghardt, K, Hanke, D. Magnetic properties of an octanuclear iron(III) cation. Inorg Chem 1993; 32: 3099-3103.
28. Castro, SL, Sun, Z, Grant, CM, Bollinger, JC, Hendrickson, DN, Christou, G. Single-molecule magnets: tetranuclear vanadium(III) complexes with butterfly structure and S = 3 ground state. J Am Chem Soc 1998; 120: 2365-2375.
29. Abragam, A, Bleaney, B. Electron paramagnetic resonance of transition ions. 1970. Clarendon Press, Oxford, UK.
30. Hagen, WR. EPR pf non-Kramers doublets in biological systems. Characterization of an S=2 system in oxidized cytochrome c oxidase. Biochim Biophys Acta 1982; 708: 82-98.
31. Calvo, R. A general spin Hamiltonian to describe ligand hyperfine structure. Ita application to heme-proteins. I. Nuclear Zeeman and hyperfine interactions. J Magn Reson 1977; 26: 445-459.
32. Pake, GE, Estle, TL. The physical principles of electron paramagnetic resonance. 1973. WA Benjamin Inc, Reading, MA.
33. Kuroda, S-I, Motokawa, M, Date, M. SH^3 term in the submillimeter electron spin resonance of cobalt tutton salt. J Phys Soc Jpn 1978; 44: 1797-1803.